

StimDust: A 2.2 mm³, implantable wireless precision neural stimulator with ultrasonic power and communication

David K. Piech^{1*}, Benjamin C. Johnson^{2,3*}, Konlin Shen¹, M. Meraj Ghanbari², Ka Yiu Li², Ryan M. Neely⁴, Joshua E. Kay², Jose M. Carmena^{2,4**}, Michel M. Maharbiz^{2,5**}, Rikky Muller^{2,5**}

¹ Department of Bioengineering, University of California, Berkeley, Berkeley, CA USA 94720

² Department of Electrical Engineering and Computer Sciences, University of California, Berkeley, Berkeley, CA USA 94720

³ Department of Electrical Engineering and Computer Engineering, Boise State University, Boise, ID USA 83725

⁴ Helen Wills Neuroscience Institute, University of California, Berkeley, Berkeley, CA USA 94720

⁵ Chan-Zuckerberg Biohub, San Francisco, CA USA 94158

Correspondence should be addressed to R.M. (rikky@berkeley.edu)

Abstract

Neural stimulation is a powerful technique for modulating physiological functions and for writing information into the nervous system as part of brain-machine interfaces. Current clinically approved neural stimulators require batteries and are many cubic centimeters in size- typically much larger than their intended targets. We present a complete wireless neural stimulation system consisting of a 2.2 mm³ wireless, batteryless, leadless implantable stimulator (the “mote”), an ultrasonic wireless link for power and bi-directional communication, and a hand-held external transceiver. The mote consists of a piezoceramic transducer, an energy storage capacitor, and a stimulator integrated circuit (IC). The IC harvests ultrasonic power with high efficiency, decodes stimulation parameter downlink data, and generates current-controlled stimulation pulses. Stimulation parameters are time-encoded on the fly through the wireless link rather than being programmed and stored on the mote, enabling complex stimulation protocols with high-temporal resolution and closed-loop capability while reducing power consumption and on-chip memory requirements. Uplink data indicates whether the mote is currently stimulating; it is encoded by the mote via backscatter modulation and is demodulated at the external transceiver. We show that the system operates at an acoustic power one fifth the FDA limit for diagnostic ultrasound and is robust to expected real-world acoustic link misalignment. We investigate

the performance of the system with motes implanted on the sciatic nerve of anesthetized rats and show highly repeatable stimulation across a wide range of physiological responses.

Extracellular electrophysiological stimulation is broadly applied to targets in the peripheral and central nervous system and has a long history of application both in neuroscience and clinical therapies. In the peripheral nervous system (PNS), the technique is well established for reinnervation of auditory sensory afferents using a cochlear implant¹. More recent work has focused on creating devices that directly stimulate the PNS to regulate physiological functions² such as modulating blood pressure³, rheumatoid arthritis⁴, incontinence⁵, sexual function⁶, and immune system function⁷; and reinnervating sensory afferents⁸ and motor efferents⁹. Electrical stimulation of central nervous system (CNS) targets is well-established for treatment of chronic pain¹⁰ and central motor disorders such as tremor in Parkinson's disease¹¹ with deep-brain stimulation (DBS). Recent work shows promising results for treatment of depression¹², modulation of decision making¹³, and use in closed-loop brain-machine interfacing^{14,15}.

The application of clinical neural stimulators to therapies with small targets deep in tissue is currently limited by implant size, implantation risk, and longevity of the device-tissue interface. Current clinically deployed neural stimulators have a volume greater than 10 cm^{3,16,17,18} and consequently must be placed in large anatomical pockets. These pockets can be far from the stimulation site (e.g., subclavical to subthalamic nucleus) or require removing substantial soft tissue or bone to form a pocket (e.g. Neuropace RNS¹⁸). Long leads are required from the stimulator housing to the stimulation site, which is a major source of infection, efficacy loss, and device failure¹⁹, in addition to electromagnetic interference, crosstalk, and power inefficiencies. Peripheral nerve cuffs which use wires to connect to a distant stimulator implant have shown detrimental effects due to strain on the nerve from the wire²⁰, emphasizing the benefit of a completely untethered device. A stimulator of a couple cubic millimeters in size or less, comparable to a grain of sand, could be placed directly at the stimulation site rather than requiring leads, thus improving safety and substantially increasing access to anatomical sites. A highly miniaturized stimulator would enable ultra-minimally-invasive delivery methods such as laparoscopy or injection, reducing tissue trauma during implantation and immune response²¹.

A key challenge in developing wireless mm-scale stimulators is wireless power and communication that provides well-controlled, therapeutically relevant effects. To date, the smallest volume stimulators have been implemented with passive components, providing inefficient voltage-mode stimulation that is sensitive to received power and electrode impedance^{22,23}. Additionally, these stimulators do not have an uplink, preventing error detection or state monitoring via feedback to the external controller. Precise control of stimulation charge is important for targeting a repeatable population of cells and maintaining safety over chronic use. Neurostimulators employing integrated circuits can use active rectifiers to achieve a higher power conversion efficiency and deliver current stimulation that is independent of

received power^{24,25,26}. However, most active neurostimulators rely on a recovered clock from the high frequency wireless signal as well as programmed registers to generate stimulation waveform timing. Significant division of the recovered clock results in power overhead and programming large registers limits the dynamic programmability of the waveform. Furthermore, most of these wireless systems use electromagnetic (EM) waves for power delivery and communication, which couples inefficiently at centimeter scales deep within tissue²⁷.

Recently, ultrasound has been proposed as an efficient way to power and communicate with mm-scale implants deep in tissue²⁸, resulting in significant volume reduction for implants^{29,30,31,32}. Compared to EM at 2 GHz, ultrasound energy at 2 MHz has less attenuation through tissue (1-2 dB/cm vs. 10-12 dB/cm³³), a higher FDA limit for power flux (7.2 mW/mm² vs. 0.1 mW/mm²³⁴), and a smaller wavelength (0.75 mm vs. 25 mm) for more efficient coupling to small implants.

Here, we present a system for wireless neural stimulation that employs 2.2 mm³ leadless, wireless “StimDust” stimulation motes. The ultrasonically powered StimDust motes contain a state-of-the-art custom integrated circuit (IC). A single link from a custom external transceiver to the mote provides power and bidirectional communication, reducing volume. A custom, time-coded wireless ultrasonic protocol dynamically sets stimulation waveforms, drastically reducing mote power consumption while maintaining a high degree of timing control.

Results

System Overview

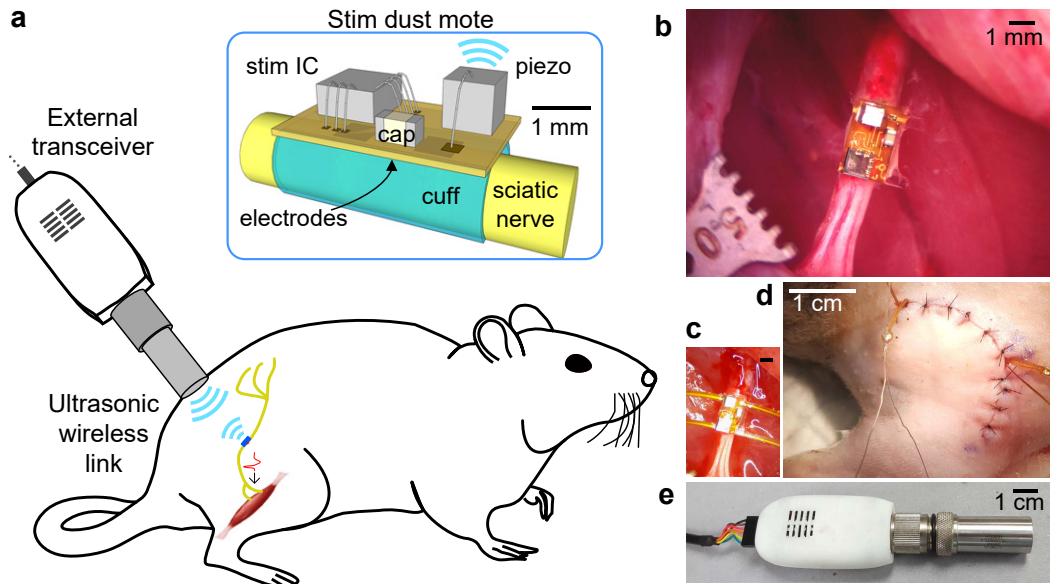


Fig. 1 | StimDust wireless neural stimulator system overview. **a**, Diagram depicting the StimDust system; here, it is used for stimulation of the sciatic nerve of a rat. **b**, The stimulating mote fully implanted and affixed to a rat sciatic nerve. Piezo at top, IC at bottom of mote. Stimulation pulses from the mote elicited compound action potentials in the nerve and compound muscle action potentials in the hindlimb musculature. **c**, Optional test leads on the mote were used for diagnostic and data reporting purposes to measure internal signals on the mote (also seen in (d)). They provided no power or control signals to the mote, and the mote function was verified with these leads disconnected from all external instrumentation. **d**, The wireless link traversed skin and muscle on top of a closed surgical site; this image shows the hindquarters of the animal superficial to the sciatic nerve. **e**, The external transceiver established an ultrasonic wireless link with the mote. The power and data cable is shown on the left and the external transducer is on the right.

A conceptual overview of the StimDust system and its implementation is shown in Fig. 1. An external transceiver (Fig. 1e) established an ultrasonic wireless link through body tissue to an implanted StimDust mote (Fig. 1b, c). A single ultrasonic link provided both power to the mote and bidirectional communication. The mote consisted of a piezoceramic as the ultrasonic transducer; a custom IC for power rectification, communication, and stimulation; a discrete capacitor for energy storage; bipolar stimulation electrodes; and a nerve cuff integrated on a thin polyimide printed circuit board (PCB). The mote was surgically implanted directly at the stimulation site, in this case the rat sciatic nerve (Fig. 1b), the wound was closed (Fig. 1d); the transcutaneous wires are optional test leads), and the external

transceiver was coupled to the outside surface of the body with ultrasound gel. The system could produce a broad set of clinically relevant stimulation currents, pulse widths, and pulse repetition frequencies (PRF); these were sufficient to elicit highly repeatable compound action potentials (CAPs) in the sciatic nerve, compound muscle action potentials (CMAPs), and associated twitches in downstream muscles.

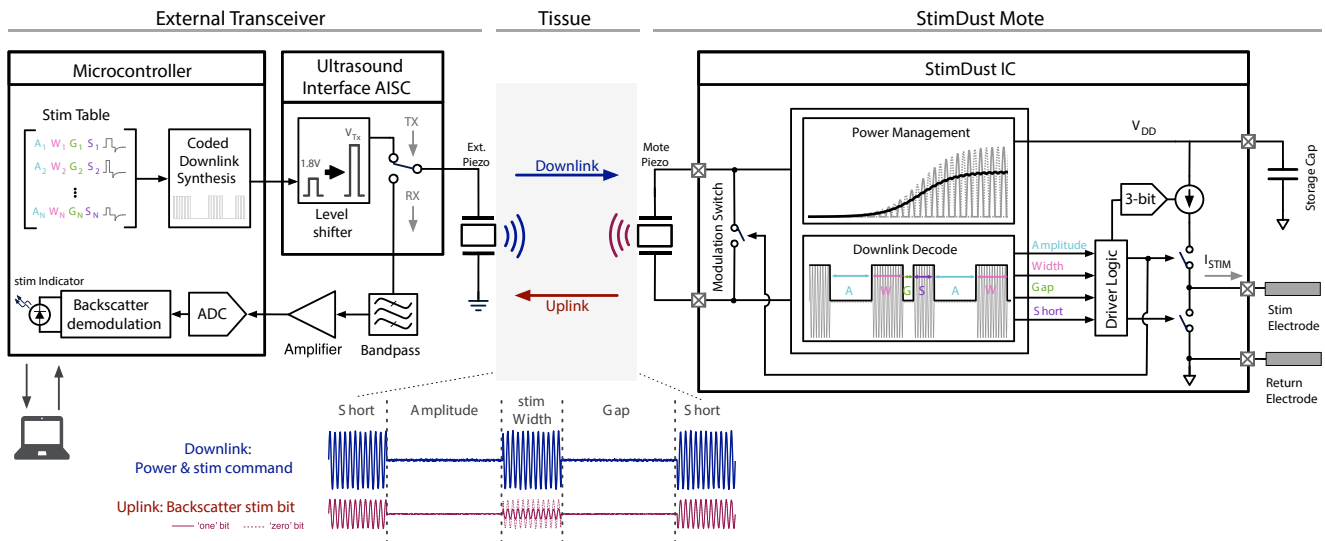


Fig. 2 | StimDust system block diagram. The external transceiver is depicted on the left, the ultrasonic wireless link in the middle, and the StimDust mote on the right. **left**, The external transceiver consisted of a transmit (Tx) path (left-top) which encoded user-specified stimulation parameters onto a 1.85 MHz carrier wave, stepped up the voltage, and drove an external piezo transducer during the Tx sequence. A receive (Rx) path (left-middle) was activated when the Tx was not active and captured and demodulated the ultrasonic backscatter. **middle**, The ultrasonic wireless link traversed the body tissue between the external transceiver and the implanted mote. The downlink provided power and time-delay coded stimulation commands for stim amplitude [A], stim pulse width [W], interphase gap duration [G], and electrode shorting duration [S]. The uplink consisted of backscatter amplitude modulation. **right**, The implanted mote harvested power and decoded stim parameters from the downlink. A finite state machine set stimulation parameters, initiated the specified stim pulse, and activated a modulation switch on the piezo input to change its ultrasound reflectance and encode a backscatter uplink bit indicating stim state information.

A functional block diagram of the system is detailed in Fig. 2. The external transceiver (Fig. 4g) utilized a microcontroller to synthesize a low-voltage transmit signal, which encoded downlink stimulation parameters for each pulse onto a 1.85 MHz carrier. The low-voltage transmit signal from the microcontroller was stepped-up in voltage and drove the external piezoelectric ultrasound transducer. During the ‘off’ periods of the transmit signal, the external transceiver toggled from Tx (transmit) to Rx (receive) mode to capture and demodulate uplink data from the acoustic signal backscattered by the mote.

The implanted mote used an IC³⁵ to rectify energy harvested by the mote’s piezo. Rectified energy was stored on an off-chip capacitor to ensure consistent operation of the IC during the ‘off’ cycles. The IC decoded received ultrasound to determine stimulation current amplitude, pulse width, interphase gap, and post-stimulation electrode shorting phase (passive recharge time). The mote delivered current-mode stimulation, during which the IC modulated the impedance across the piezo to change the amplitude of the reflected PZ wave. This indicated to the external transceiver when the IC was stimulating and operating properly.

Protocol and implant design

The IC timing diagram and architecture are shown in Fig. 3a, b. The IC used a custom ultrasound protocol, which enabled dynamically controlled stimulation waveforms and high system efficiency while maintaining a high degree of timing control. The protocol utilized the shape of the incoming ultrasound envelope to encode stimulation parameters, eliminating the need for an on-chip, continuously running clock to ensure timing precision. This reduced power consumption and afforded greater stimulation waveform timing flexibility compared to solutions that rely on a clock receiver, divider circuits, and on-chip registers to generate the stimulation waveform^{36,24}.

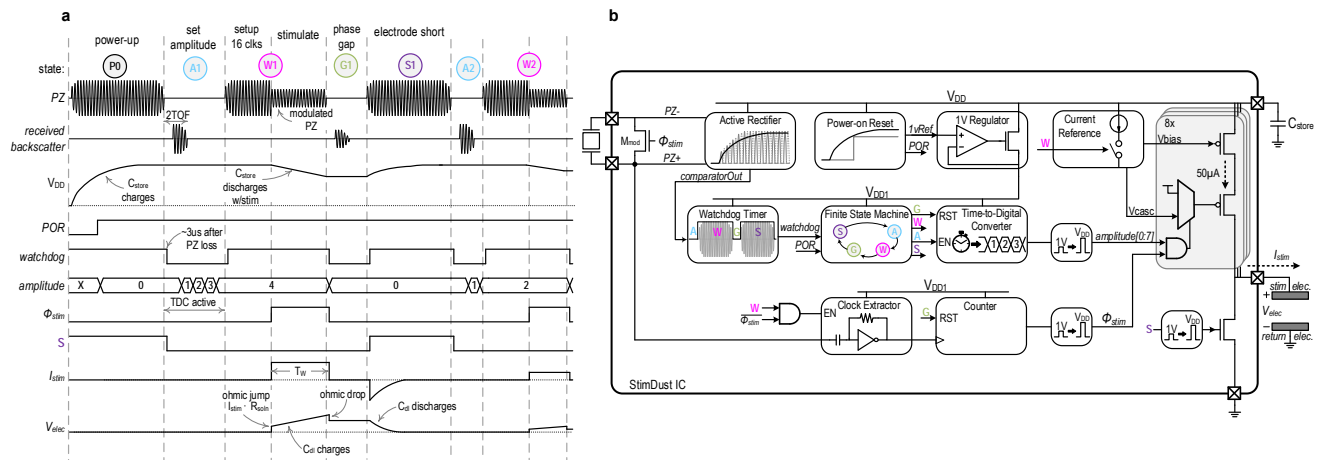


Fig. 3 | StimDust IC. **a**, The IC timing diagram and **b**, architecture. Ultrasound from the external transducer charged VDD and the POR initialized the system. The watchdog detected ultrasound-free intervals and incremented the state. The amplitude was set by the duration of state A via a time-to-digital converter. Φ_{stim} enabled the stimulation current, I_{stim} , and the modulation switch, M_{mod} . Backscattered ultrasound was detected by the external transducer during the ultrasound-free intervals. IC circuitry was heavily duty-cycled to conserve power.

As shown in Fig. 3, an initial power-up sequence charged the implant's storage capacitor, C_{store} . As the supply voltage of the IC (V_{DD}) ramped up to 2.5 V, a power-on-reset (POR) signal (threshold ≈ 1.6 V) was generated to initialize the chip. If the POR signal was not generated, or V_{DD} dropped below the threshold, the IC would not stimulate as a fail-safe against aberrant stimulation. In addition to the power-up sequence, the protocol was comprised of 4 repeating states: set amplitude (**A**), pulse width (**W**), interphase gap (**G**), and electrode shorting (**S**). Every state encoded information pertinent to the stimulation waveform interpreted by the IC and had a temporal resolution set by the carrier frequency ($1/f_{\text{carrier}} = 540$ ns). States **A** and **G** are called ultrasound-free intervals (UFI). **A** occurred during the first UFI and its duration encoded the stimulation amplitude. The watchdog timer circuit detected the UFI, which then triggered a 3-bit time-to-digital converter (TDC). The 3-bits of the TDC output were stored in memory for the stimulation pulse amplitude. **W** began when ultrasound returned and started a 16-cycle setup sequence to allow the current reference to settle prior to stimulation. On the 16th cycle, a current mirror whose amplitude was set by the TDC was enabled by the output of the counter, Φ_{stim} , causing current to flow from the stimulation electrode to the return electrode.

Stimulation was terminated at the second UFI. During **G**, the chip was in standby mode and the stimulation electrode was tri-stated to create an interphase gap. Interphase gaps have been shown to decrease stimulation thresholds in auditory nerves, motor nerves, and retinal ganglion cells, in addition to decreasing perceptual thresholds in cochlear implant patients and epiretinal prosthesis patients^{37,38}. State **S** started when ultrasound returned. During **S**, received ultrasound recharged the storage capacitor and the IC shorted the stimulation electrode to ground, clearing accumulated charge on the electrodes. Since the charge cleared quickly, passive recharge³⁹ was favorable to conventional biphasic stimulation since it consumes half the energy without limiting stimulation frequency in this work. Furthermore, biphasic stimulators typically use an additional shorting phase to clear residual charge that accumulates from phase mismatch.

Whenever ultrasound was on (**W** and **S**), a fraction of the incident ultrasonic energy was reflected to the external transceiver (backscatter). The backscatter amplitude was a function of the electrical load of the mote piezo. The delay between transceiver emission and backscatter detection was twice the acoustic time-of-flight (~ 20 - $60\mu\text{s}$) between the external transducer and the mote piezo. During stimulation, a transistor switch, M_{mod} (Fig. 3b), was turned on to create a weak short (~ 4 k Ω) across the piezo terminals, reducing the amplitude of the backscatter signal (Supplementary Fig. 1). When M_{mod} was off, the electrical load impedance across the piezo ranged from 10 k Ω to 300 k Ω depending on the power consumption of the IC. The impedance change during stimulation provided a 1-bit data uplink and safety indicator, informing the external transducer when the mote was stimulating.

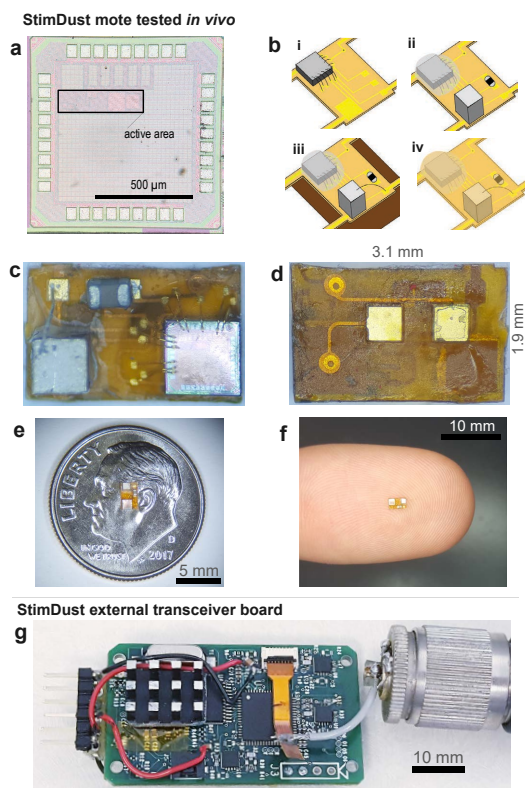


Fig. 4 | StimDust fabrication. **a**, Mote IC die photo. **b**, Mote fabrication steps: (i) IC die was wire-bonded to mote flex substrate; (ii) discrete capacitor and piezo were bonded with silver epoxy and die was encapsulated with epoxy; (iii) piezo was wire-bonded; (iv) mote was encapsulated with parylene. **c**, Top view of mote: piezo on left, capacitor at top, IC on right. **d**, Underside view of mote: ground electrode on left, working electrode on right. **e**, Size comparison to US dime and **f**, a finger. **g**, External transceiver board. Data and power connection is on the left, microcontroller is under the passive heat sink, ultrasound interface chip is middle-right and transducer connector on the right.

StimDust motes (Fig. 4) consisted of the IC, external storage capacitor, and a $750\ \mu\text{m} \times 750\ \mu\text{m} \times 750\ \mu\text{m}$ lead-zirconate titanate (PZT) piezoceramic transducer attached to a miniature flexible PCB and encapsulated with parylene. The piezo thickness was chosen such that the series resonance was at the carrier frequency of 1.85 MHz. This choice of thickness and carrier frequency was a trade-off between improving voltage harvest (larger thickness), lessening the effect of higher ultrasound attenuation at higher frequencies (lower carrier frequency), and reducing mote size (smaller thickness). The piezo thickness-to-width ratio (1:1) was a trade-off between improving current harvest (larger surface area), minimizing mote size (smaller surface area), and increasing ultrasound acceptance angle (smaller aspect ratio). Stimulation electrodes located on the bottom of the PCB were electroplated with poly(3,4-

ethylenedioxythiophene) polystyrene sulfonate (PEDOT:PSS) to bring impedance down to 4 k Ω at 2.5 kHz and prevent compliance limiting when using the full current range of the chip.

The completed StimDust mote had maximal dimensions of 3.1 mm length, 1.9 mm width, and 0.89 mm height. The mote volume was 2.2 mm³, the convex hull volume was 3.6 mm³, and the rectangular bounding box volume was 5.3 mm³. For comparison, current deep brain stimulation *electrodes* are 1.27 mm in diameter, > 7 mm in active length and >70 mm in implanted length^{40,41}. A more aggressively scaled mote of 0.65 mm³ in volume was also designed (Supplementary Fig. 2) which used the same system architecture, piezo size, and fabrication techniques. The 2.2 mm³ mote design was used for all experiments reported in this paper, but the 0.65 mm³ mote design had no expected difference in performance.

Robust wireless operation in a gel tissue phantom

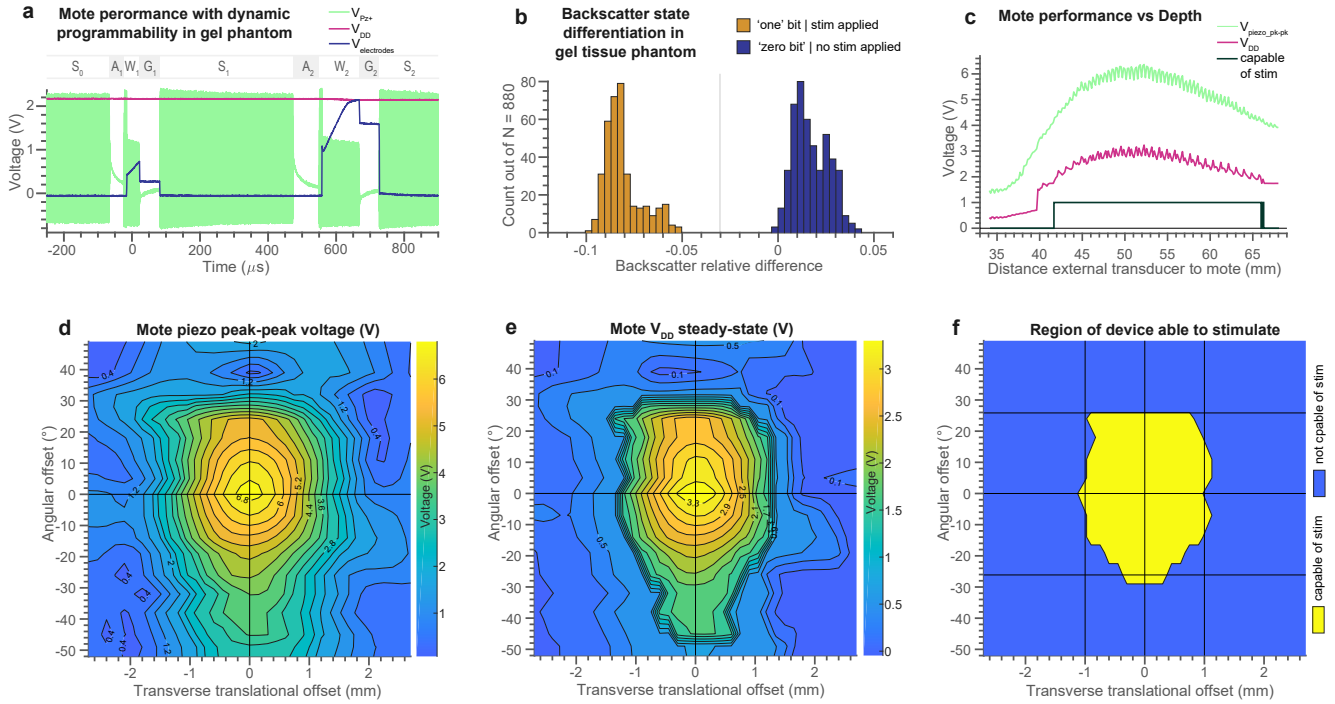


Fig. 5 | StimDust performance in gel tissue phantom. **a**, Mote waveforms recorded during a representative stimulation sequence where stimulation parameters were changed on-the-fly, demonstrating dynamic programmability. The first stimulation pulse of $150\ \mu\text{A}$ for $37\ \mu\text{s}$ was specified by regions A_1 , W_1 , and G_1 . The second stimulation pulse of $300\ \mu\text{A}$ for $110\ \mu\text{s}$ was specified by A_2 , W_2 , and G_2 . These two different dynamically-encoded pulses are less than $500\ \mu\text{s}$ apart. **b**, Backscatter relative difference (see Methods) for 916 stimulation pulses. A population of successful stim pulses with backscatter values of ‘one’ bits was taken under good mote operating conditions with verified stim at the outputs. A population of backscatter samples with no stim and backscatter values of ‘zero’ bits was acquired by operating the mote in an underpowered state such that output stimulation was no longer performed. The two populations show good separation, enabling the use of backscatter as an indicator of successful stimulation. **c**, A mote was operated while its depth was scanned relative to a fixed external transducer acoustic field, yielding a viable region in depth. This was performed with the $25.4\ \text{mm}$ diameter external transducer at $31.5\ V_{\text{pk-pk}}$ transmit. **d**, **e**, **f**, A mote was operated within a fixed external transducer acoustic field while its position and orientation were scanned across transverse offset and angular offset relative to the mote central axis. Depth was held constant at $48\ \text{mm}$. **d**, Mote piezo harvest voltage. **e**, Mote regulated voltage. **f**, Mote able to stimulate region.

The error between specified current output and actual current output across all 8 amplitude levels ($50\ \mu\text{A}$ to $400\ \mu\text{A}$) was 2.0% on average and 8.1% maximum (maximum absolute current error of $5.7\ \mu\text{A}$). The system achieved up to $2.38\ \text{kHz}$ pulse repetition frequency (PRF) while stimulating with a pulse width of $80\ \mu\text{s}$ at $400\ \mu\text{A}$ and minimal compliance limiting. A PRF of $5.05\ \text{kHz}$ was achieved with $50\ \mu\text{A}$ current and $80\ \mu\text{s}$ pulse width. Higher frequencies resulted in a V_{DD} droop and compliance-limited

current output, though absolute maximum PRF was 16 kHz. Piezo impedance modulation via the M_{mod} switch for uplink data modulation showed a drastic amplitude change in V_{Pz+} (Fig. 5a). At the external transceiver, the actual uplink bit error rate (BER) (Fig. 5b) was 0 out of 880 and the estimated Gaussian fit BER was 9.9×10^{-8} .

The minimum acoustic field peak intensity under which the mote could power up and stimulate was 142 mW/cm^2 derated I_{SPTA} with a mechanical index of 0.049 (pressure amplitude of 66.1 kPa), 20% and 2.6%, respectively, of the FDA limits for diagnostic ultrasound³⁴. While keeping derated I_{SPTA} at the FDA limit, a mote operating in a gel tissue phantom achieved a stimulation of $89 \text{ }\mu\text{W}$ (23 nC and 37 nJ per pulse at 2380 Hz), and the power efficiency from acoustic domain to applied electrical stimulation power was 1.9% (Supplementary Section 1 and Supplementary Table 1).

The use of an ultrasonic link over an EM one was crucial for achieving high link efficiencies at sub-mm transducer sizes and cm-depths in tissue. An important consideration for the practical deployment of such a system is understanding the effect of acoustic link alignment. The StimDust system could reliably operate when the mote was shallower than 66 mm (70 mm absolute maximum operational depth observed), when the incident ultrasound was within $\pm 25^\circ$ of the mote central axis, and when the external beam was centered within a 2.2 mm range around the mote position (Fig. 5c-f). Depth and lateral alignment of the mote within the external transceiver acoustic beam were easily controlled by adjusting the position, angle and skin-offset of the external transceiver. The mote's precise angular orientation within the tissue, on the other hand, was difficult to measure, constrain, and control after implantation; the relatively wide $\pm 25^\circ$ acceptance angle enabled a robust acoustic link despite this fact.

Attenuation in body tissues is greater than that of ultrasound gel, reducing the maximum depth of operation. In fat, liver, and muscle tissue (1.1 dB/cm, 1.78 dB/cm, 2.2 dB/cm attenuation, respectively, at 1.85 MHz^{42,43}), the maximum depth of operation is estimated to be 62 mm, 56 mm, and 51 mm, respectively. These distances can be improved by using an external transducer with longer focal length and larger diameter.

Precise stimulation *in vivo*

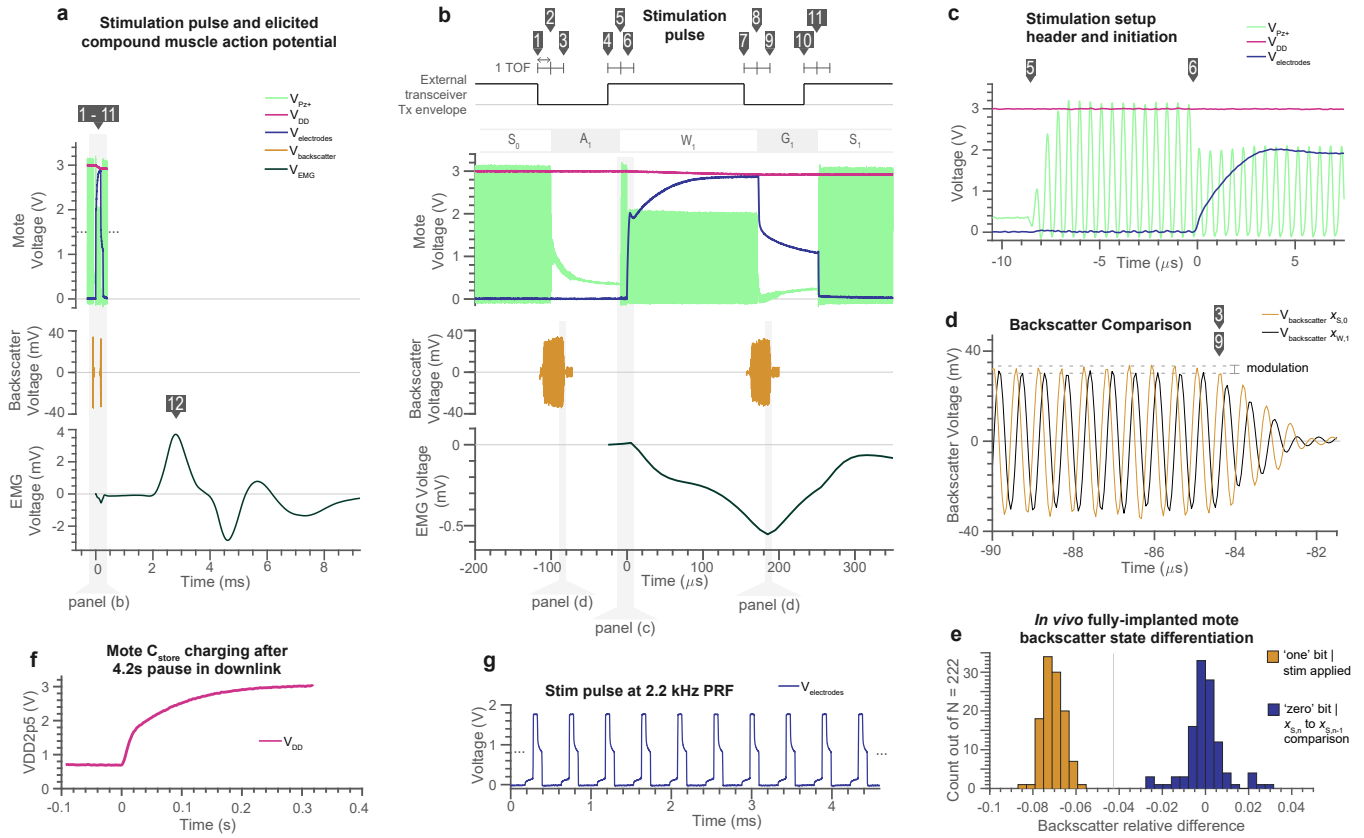


Fig. 6 | *In vivo* performance: mote, backscatter, and evoked neural response waveforms for fully-implanted mote. **a**, A stimulation pulse from the mote (a top) elicited a compound muscle action potential (a bottom). **b**, Detail of stimulation pulse signals. The downlink code regions A_1 , W_1 , and G_1 specify the stimulation pulse. During S_0 the ultrasound envelope was high (V_{pz+}), the charge in the energy storage capacitor was topped off (V_{DD}), and the electrodes were shorted (V_{elec}). [1] The external interrogator set the downlink ultrasound envelope from on to off, and after a short delay, began to capture the backscatter signal $x_{S,0}$ from the mote from the S_0 period ((b), middle). [2] One acoustic time-of-flight (TOF, approximately 16.9 μs in this trial) later the mote saw a transition from S_0 to A_1 , beginning the first UFI (ultrasound free interval) and initiating the current amplitude TDC decoder. [3] One TOF after the mote S_0 to A_1 transition, the primary backscatter from the mote S_0 region as seen at the external transducer ceased ((d), orange line). [5] At the mote A_1 to W_1 transition, the stimulation amplitude was set, and a header / setup sequence lasted for 16 ultrasound cycles (c), after which [6] the stimulation output pulse began and M_{mod} turned on, reducing the amplitude of $V_{pz+/-}$. During stimulation, the voltage measured at the stimulation electrodes showed an immediate $I_{stim} \cdot R_{soln}$ increase, and then gradually increased due to charging of the double layer capacitance. V_{DD} dropped linearly during this period due to constant current flow through the stimulation electrodes. In addition, there was an electrical stimulation artifact on the EMG signal during the stimulation event ((b), bottom). [7] The external transceiver began the second UFI and after a short delay, began to capture the backscatter signal $x_{W,1}$ from the mote from the W_1 period ((b), middle). [8] At the mote W_1 to G_1 transition, the stimulation electrodes were set to high impedance for the interphase gap. The electrode voltage showed an immediate $I_{stim} \cdot R_{soln}$ drop and then a $R_{soln} \cdot C_{dl}$ discharge as the double-layer capacitance discharged. [9] One TOF later the primary backscatter seen at the external transceiver from the W_1 period ceased ((d), black line). [11] At the mote G_1 to S_1 transition, the stimulation electrodes were shorted to

discharge any remaining charge. [12] The stimulation pulse produced by this sequence of events evoked the compound muscle action potential seen in (a, bottom). **d**, Detail of backscatter signal captured at external transceiver, showing amplitude modulation. **e**, The two regions from (d) were compared to yield 111 ‘one’ bits, with good separation from 111 ‘zero’ bits. **f**, Initial charge-up of the $4\ \mu\text{F}$ C_{store} after the mote had been without power for 4.2 seconds and V_{DD} had drained to 0.7 V. **g**, High pulse repetition frequency in-vivo stimulation. The small electrode voltage rise which precedes the main ohmic rise in each of these pulses is due to the remaining charge on the stimulation electrodes from the previous stimulation pulse which was not fully cleared during relatively brief $\sim 230\ \mu\text{s}$ shorting phase. Note: data in panels (a-e) are from the same stimulation parameters condition during a single *in vivo* experiment with a fully implanted mote. Data in panel (f) is from *in vivo* fully-implanted mote. Data in panel (g) is from *in vivo* while taking data with an open surgical site.

In vivo stimulation elicited robust and repeatable compound action potentials and was demonstrated across four different motes. Two of the motes had overlaying tissue flaps replaced and sutured after implantation and were operated through tissue (Fig. 6, Supplementary Video 1). The acoustic field (Supplementary Fig. 3) had a derated I_{SPPA} and I_{SPTA} of $713\ \text{mW}/\text{cm}^2$ and mechanical index of 0.11, both below the FDA limits of $720\ \text{mW}/\text{cm}^2$ and 1.9, respectively, for ultrasound diagnostic imaging³⁴, and lower than thresholds for directly ultrasound-mediated stimulation (Supplementary Section 2). Fig. 7a-d shows all signals of interest during a stimulation pulse while a fully implanted mote was operated through skin and muscle layers. The downlink commands received by the mote, S_0 , A_1 , W_1 , G_1 , S_1 , can be seen in the $V_{\text{Pz+}}$ trace in figure 7(b), top. The conduction delay between stimulation and evoked CMAP of approximately 1.5 ms corresponded to the expected conduction velocity of approximately $25\ \text{m/s}$ ⁴⁴ and distance of approximately 30 mm. Through-tissue backscatter uplink performance (Fig. 6d, e) had an actual BER of 0 out of 222 and a gaussian fit estimated BER of 1.5×10^{-7} . This indicated a robust 1-bit data uplink that could reliably report the success of each pulse to the user.

Stimulation parameters control physiological response

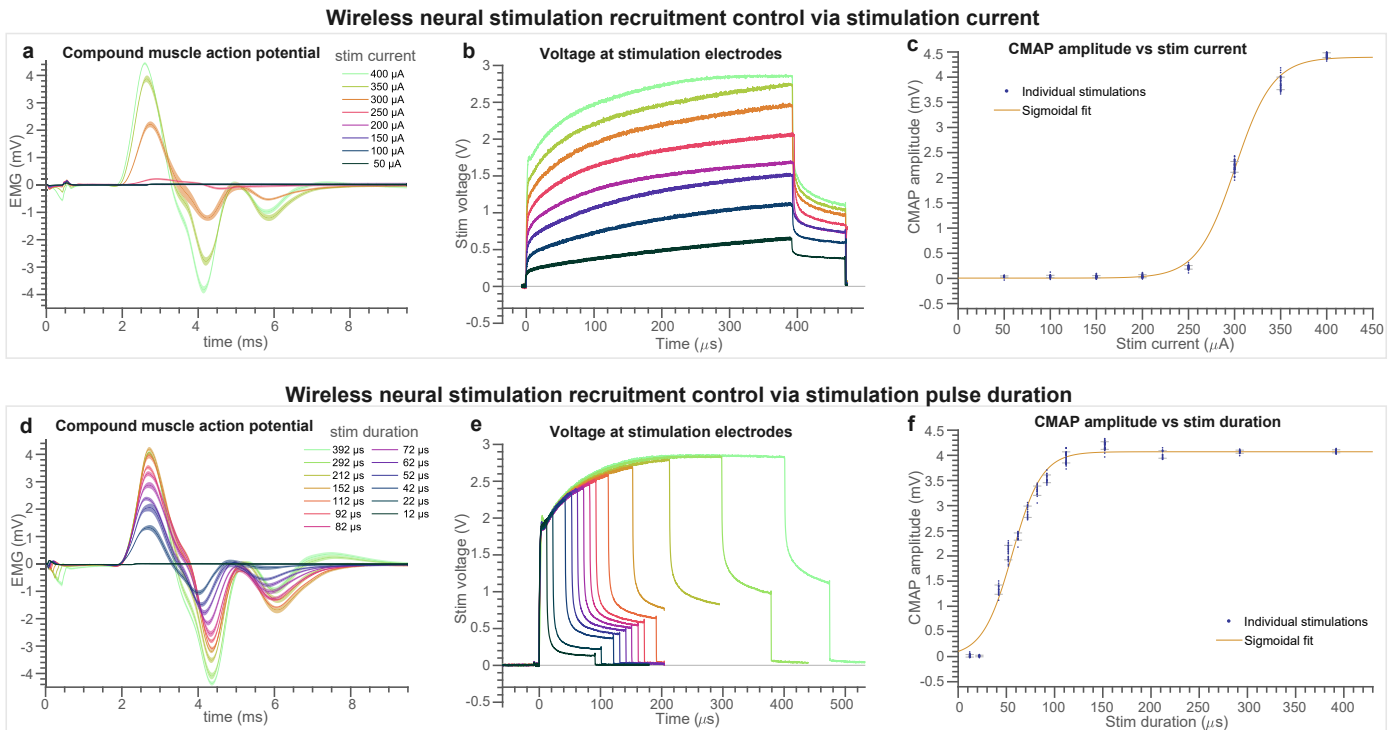


Fig. 7 | Precise control of evoked neural response achieved through varying stimulation current or stimulation pulse width. [Current-control]: Stimulation current was varied from 50 μA to 400 μA with stimulation pulse width held at 392 μs . **a**, CMAP (compound muscle action potential) waveforms show activation for 250 μA to 400 μA . The width of the lines (shaded error regions) are $\pm 1\sigma$ (between 21 and 64 pulses per condition). **b**, Stimulation electrode voltage shows an approximately linear trend with stimulation current. **c**, CMAP amplitude vs. stim current shows a typical sigmoidal recruitment curve. Line is sigmoidal fit and error bars are $\pm 1\sigma$. **[Pulse-width-control]:** Stimulation pulse width was varied from 12 μs to 392 μs with stimulation current held at 400 μA . **d**, CMAP waveforms show activation from 42 μs to 392 μs . The width of the lines (shaded error regions) are $\pm 1\sigma$. This panel shows that the duration of the electrical artifact increased with increasing stimulation pulse width, but the time-course of the CMAP did not appreciably change, with only amplitude differing. **e**, Stimulation electrode voltage show similar dynamics for increasing stimulation pulse width. **f**, CMAP amplitude vs. stim pulse width shows a typical sigmoidal recruitment curve with little or no evoked response below 22 μs pulse width and saturation at approximately 140 μs pulse width. Line is sigmoidal fit and error bars are $\pm 1\sigma$. Note: This data was taken with an open surgical site.

In vivo EMG response was controlled by varying stimulation current from 50 μA to 400 μA with fixed 392 μs pulse width (Fig. 7a-c). The low standard deviation of the CMAP waveforms (line width in Fig. 7a, d) indicated highly repeatable stimulation and biological response across pulses. The recruitment curve as a function of stimulation current (Fig. 7c) showed a threshold of activation between 200 μA and 250 μA and saturation between 350 μA and 400 μA . The CMAP amplitude saturated at 4.4 mV. *In vivo* EMG response was also controlled by varying stimulation pulse width with fixed 400 μA

current (Fig. 7d-f). The CMAP amplitude response showed the duration-threshold of elicitation of action potential at 400 μA current to be approximately 26 μs , with response saturation around 150 μs and maximum CMAP amplitude of 4.2 mV.

A second set of current-control and pulse-width-control sweeps were performed two hours after the first (Supplementary Fig. 5). Wireless link performance, communications, and stimulation output were unchanged. The biological response was very similar but showed recruitment curves shifted slightly left, indicating a 15% reduced threshold of recruitment, and 11% lower CMAP amplitude saturation. These slight differences were potentially due to impedance changes at the electrodes and excitability in the nerve as the tissue began to respond to the implant, muscle fatigue (though pulse repetition frequency was low), or changes in the plane of anesthesia.

In vivo stimulation across pulse repetition frequencies from 0.22 Hz to 2.22 kHz yielded four regimes of muscle activation. Pulse width and current were fixed at 52 μs and 400 μA . By visually observing muscle twitch response, we qualitatively reported single twitches at 0.25, 0.33, 1, 2, 5, and 10 Hz, unfused tetanus at 32 Hz, and fused tetanus at 100 and 320 Hz. This matched expected muscle responses for rat gastrocnemius⁴⁵. At 2 kHz and 2.22 kHz (Fig. 6g), we observed a single initial twitch and then apparent relaxation. While we did not measure muscle force in this study and thus could not positively confirm nerve block, nerve block has been reported at 2 kHz stimulation frequency and 1 V drive voltage (approximately 666 μA)⁴⁶. Therefore, while not conclusive, these observations were consistent with the system performing nerve block.

Discussion

Our results indicated that repeatable, controlled compound action potentials can be elicited by the StimDust system. Grading the physiological response through controlling stimulation current, pulse-width, and pulse repetition frequency demonstrated efficacy for a wide range of stimulation techniques and is an important component of safety. Furthermore, miniaturization of the precision stimulator enabled placement directly at the stimulation site *on* the sciatic nerve.

Table 1: State-of-the-art comparisons table

	TBioCAS '18 [32]	TCAS II '13 [31]	PLOS ONE '17 [22]	Sci. Reports '18 [25]	Front. Neuro. '17 [23]	TBioCAS '18 [47]	StimDust This Work
Stim. type	current	current	voltage	current	voltage	current	current
Link	ultrasound	ultrasound	RF	4 coil inductive	RF	RF	ultrasound
f_{carrier} [MHz]	1.3	1	2400	13.56	10	1300	1.85
Uplink	none	none	none	433 MHz OOK	none	none	backscatter
Process [nm]	180HV	350	discrete	130	discrete	130	65
Waveform configuration	digital bitstream	digital bitstream	received power	digital bitstream	received power	received power	envelope detection
F_{stim} [Hz] / resol. [bit]	0 - 60	60 - 265 / 2b	0 - 25*	13-414 / 5b	2*	0 - 3*	0 - 5k**
Stim start	enable signal	--	received power	stim command	received power	received power	enable signal
T_{pulse} resolution [us]	14 / 5b	200 / fixed	continuous	9.5 / 5b	continuous	continuous	continuous
$I_{\text{stim,max}}$ [μ A] / resol. [bit]	5000 / 8b	640 / 5b	undefined	1860 / 5b	undefined	25 / fixed	400 / 3b
T_{gap} resolution [μ s]	1/2 T_{pulse}	--	N/A	9.5 / 5b	N/A	N/A	continuous
Charge balance	biphasic/gnd	dc-blocking cap	none	3b biphasic correction	none	none	passive recharge
Compliance voltage (V)	15	3.3	N/A	2	N/A	1.2	3
Animal model	ex-vivo frog sciatic		pig vagus	rat sciatic	rat sciatic	ex-vivo rat sciatic	rat sciatic
Fully-implanted	no	no	yes	yes	yes	no	yes
in-vitro depth _{tx-rx} [mm]	105 (castor oil)	--	--	--	--	5	70 (gel), 51 (muscle)
in-vivo depth _{tx-rx} [mm]	--	50	15	--	50	--	20
Mass [mg]	78	--	300	2800	--	--	10
Circuit η ($P_{\text{stim}}/P_{\text{in}}$) [%]	<50	--	20	--	--	--	82
Volume [mm ³]	39	1020	40.5 [†]	2250	0.45 [‡]	--	2.2[‡]
Electrodes [mm]	0.5 \emptyset x 2.0 Pt cylinder	--	2.7 \emptyset x 1.0 Pt cuff	cuff	0.3 \emptyset Pt disk	0.125 \emptyset SS disk on cuff	0.55 PEDOT square
Implant encapsulation	PDMS	--	epoxy	epoxy & PDMS	epoxy	--	parylene
FOM (Depth/Volume)	2.69	0.05	0.37	--	111.11	--	23.18\S
FOM (Volume/Efficiency)	0.78	--	2.03	--	--	--	0.03

*demonstrated, range not provided

[†]estimated

**up to 16kHz in burst

[‡]includes stim electrodes

Table 1 summarizes the performance of StimDust and compares it with state-of-the-art implantable wireless neural stimulators^{32,31,22,25,23,47}. Wireless ultrasonic power and data delivery enabled implant operation at a depth of 70 mm in ultrasound gel. Additionally, direct control of the stimulation waveform by the received ultrasound boasted several advantages over state-of-the-art. Compared to systems that program notes via a bitstream, StimDust achieved sub- μ s ($1/f_{\text{carrier}}$) temporal resolution with a larger dynamic range for pulse width, interphase gap, and PRF because the complexity was pushed to the external transceiver, which had fewer computational and power constraints. Stimulators which used only passive components^{22,23} used a direct control scheme as well; however, the stimulation intensity was dictated by the received power and the output was voltage stimulation which is sensitive to electrode properties. Furthermore, they did not feature an uplink whereas StimDust included a wireless uplink via ultrasonic backscatter for safety monitoring and alignment. Active rectification increased efficiency and established a ground reference potential, enabling StimDust to use passive recharge to save power relative to biphasic stimulation while clearing residual stimulation charge on the electrodes, which other direct control systems^{22,23} were unable to do. Using an enable signal, or

stimulation start command, allowed the mote to stimulate with low latency, which is crucial for closed-loop experimentation.

In addition to highly programmable stimulation, StimDust was also the smallest neural stimulator with precise current-control output. The efficient integration and co-design of the piezoceramic, StimDust IC, storage capacitor, and interface electrodes enabled miniaturization of the mote down to 2.2 mm^3 in volume and 10 mg. This represents $>10x$ improvement in depth/volume figure of merit (FoM) and $>25x$ improvement in volume/efficiency FoM relative to other state-of-the-art precision neural stimulators. A further-miniaturized revised StimDust design yielded a mote volume of 0.65 mm^3 and expected depth/volume FoM of 78 mm^{-2} , a $>29x$ improvement over state-of-the-art.

The use of ultrasound as the wireless power carrier enabled direct voltage harvest from the mote piezo of up to $\sim 7 \text{ V}_{\text{pk-pk}}$ and $\sim 3.5 \text{ V}$ rectified under safe ultrasound intensity levels, which is sufficient for stimulation with low-impedance electrodes. We chose to take advantage of this to optimize for high power-efficiency rectification. While operating at clinically relevant depths of multiple centimeters, this enabled our high PRF (and high total $P_{\text{stimulation}}$), which is important for some clinical use cases such as nerve block. The acoustic-to-electrical power conversion could have alternatively been optimized for voltage efficiency rather than power efficiency which would have enabled greater depth of operation or a thinner piezo (both of which reduce mote piezo voltage) at the expense of maximum PRF and $P_{\text{stimulation}}$.

An important use case for a wireless neural stimulator is placing the mote in the brain for use in DBS and brain-machine interfacing. While establishing an ultrasonic power and communications link through the skull is challenging due to the greater attenuation in skull than in soft tissues, transcranial ultrasound has been shown to safely achieve ultrasonic power levels in the brain of 159 mW/cm^2 at 2 MHz and a focal depth of 4.5 cm ^{48,49}. StimDust is able to operate at a power level (142 mW/cm^2) and frequency (1.85 MHz) lower than this, indicating applicability to transcranial and deep-brain operation.

We have introduced the smallest wireless neural stimulator that can deliver current-controlled stimulation. Compact mote integration and programmable stimulation was enabled by a custom wireless ultrasound protocol and an energy efficient integrated circuit. We demonstrated its use fully implanted in anesthetized rats to controllably elicit compound action potentials across a range of clinically relevant stimulation regimes. Taken together, this work shows a practical demonstration of a stimulator for the PNS with potential applicability to the CNS. We anticipate the introduction of a new class of neural stimulators that are small enough to be deployed en masse with low risk to the patient, and which open up new and powerful therapeutic and neural interface techniques.

Methods

Design, fabrication, and assembly of the StimDust motes: The StimDust motes were built on a 100 μm thick, polyimide, flexible PCB (Altaflex, Santa Clara, CA). Polyimide substrates were preferable to FR-4 substrates due to their higher thermal budget, superior chemical compatibility with organic solvents, and higher flexibility of the substrate, facilitating device testing and *in vivo* implantation.

Stimulation electrodes were located on the underside of the PCB. The electrodes had 0.55 mm x 0.55 mm dimensions with 1 mm center-to-center spacing. To prevent compliance limiting when using the full current range of the chip, the electrode impedances were designed to be $< 6.25 \text{ k}\Omega$ at the stimulation pulse frequency ($\sim 2.5 \text{ kHz}$ for a pulse width of 200 μs – the lowest frequency used and therefore highest impedance). The impedance of the gold electrodes on the PCB was lowered by electroplating poly(3,4-ethylenedioxythiophene) polystyrene sulfonate (PEDOT:PSS) using a NanoZ impedance testing and electroplating device (White Matter LLC, Mercer Island, WA). In recent work, PEDOT:PSS has demonstrated a charge injection limit 15x that of PtIr and IrOx electrodes and $>3\text{x}$ reduction in the voltage transient⁵⁰. The impedance of the gold stimulation electrodes was characterized in 1x phosphate buffered saline (PBS) using a NanoZ before and after PEDOT plating and again after full assembly of the motes. One electrode served as the active electrode while the other served as the reference electrode. A frequency sweep between 1 Hz and 5.02 kHz was performed and the impedance data collected, yielding an impedance of approximately 4 k Ω at 2.5 kHz³⁵.

Following electroplating, the IC was attached to the PCB using a conductive silver epoxy (H20E, Epoxy Technology Inc., Billerica, MA) (Fig. 4b) and cured at 150 $^{\circ}\text{C}$ for 10 minutes. The IC and PCB were then cleaned in acetone, followed by isopropyl alcohol and DI water to clean the device prior to wirebonding. The IC was wirebonded to the PCB using an ultrasonic wedge wirebonder (7400B, West Bond, Scotts Valley, CA) and potted in UV-curable epoxy (AA 3526, Loctite, Düsseldorf, Germany) to protect the wirebonds.

Next, a 750 μm x 750 μm x 750 μm lead-zirconate titanate (PZT) cube (841, APC Int., Mackeyville, PA) and an 0201 surface mount capacitor for charge storage were attached to the PCB using silver epoxy and cured at 150 $^{\circ}\text{C}$ for 10 minutes. PZT was chosen for its high electromechanical coupling constant and relatively low loss tangent enabling good voltage and power harvest in semi-continuous-

wave applications. Barium titanate piezoceramic could also be used for improved biocompatibility, but with a slight reduction in electromechanical coupling coefficient. The PZT coupon was diced from a 750 μm thick sheet of PZT, premetallized with 12 μm of fired-on silver, using a wafer-dicing saw with a ceramic-cutting blade. To complete the circuit, the top terminal of the PZT coupon was wirebonded to the PCB.

The devices were then coated with roughly 10 μm of parylene-C for insulation using chemical vapor deposition (Specialty Coating Systems, Indianapolis, IN). Parylene was chosen as the insulation material due to its excellent properties as a moisture and chemical barrier⁵¹. Furthermore, because parylene can be precisely deposited with thicknesses on the order of microns, it does not damp the vibrations of the piezoceramic as strongly as other insulation materials such as polydimethylsiloxane (PDMS) or epoxy, allowing for higher efficiency power harvesting. The stimulation electrodes were exposed by gently scoring the parylene around the electrodes using a tungsten probe tip and peeling the parylene away. The parylene encapsulation used in this work is expected to last from several months to a few years in the biological environment⁵². Implementation of recent advances for long-term conformal encapsulation for mm-scale implantable devices could enable decades- or lifetime-longevity^{53,54}.

To aid in surgical placement of the mote on the rat sciatic nerve, a cuff was affixed to the back of the mote. The cuff was made by cutting a small piece of silicone tubing (0.8 mm ID, 1.6 mm OD) to roughly the length of the mote. The tubing was then cut in half and attached next to the electrodes using UV-curable epoxy and silicone adhesive.

A further-miniaturized revision of the StimDust mote was also designed (Supplementary Fig. 2). For this design, an IC was fabricated with its size reduced by removing unnecessary test circuits and debug pads and using pad-over-circuit. Additional size reduction in the mote design came from the use of a 0.5 mm x 0.25 mm footprint storage capacitor and refinement of component and wirebond placement. While this smaller design was not used for the experiments reported in this paper, it did achieve a size with maximal dimensions of 1.17 mm length, 0.77 mm width, 0.89 mm height, 0.65 mm³ volume, 0.7 mm³ convex hull volume, and 0.8 mm³ rectangular bounding box volume. This design is substantially smaller than the tip of a DBS lead.

Design of the external transceiver: The external transceiver was a compact device designed to be held by a user with its ultrasonic transducer head placed against the skin of a subject. A previous version demonstrated that the external transceiver could also be configured as a wearable device with a low-

profile transducer⁵⁵. The transceiver established an ultrasonic wireless link with the mote to provide power, control stimulation parameters via time-coded downlink data, and report back whether the mote had successfully applied each stimulation pulse via detecting backscatter modulation. It was designed around two major components: a high-performance microcontroller (NXP LPC4370) for system control and digital modulation / demodulation, and a custom ultrasound interface IC⁵⁶. Due to the relatively low frequencies used, a full-digital transceiver was implemented with direct digital synthesis of the transmit signal and digitization of the raw receive signal, enabling greater modulation / demodulation design flexibility.

Signal flow through the transceiver is depicted in Fig. 2. A stimulation protocol was programmed into the system and stored in a stimulation table as a sequence of A, W, G, S duration values for each stimulation event. This table could store up to 4500 unique stimulation events of differing parameters and is repeated. An on-board PLL generated a 1.85 MHz square wave carrier signal. On-board timers utilized the stimulation table data to encode the downlink timing with on-off keying onto the carrier signal with sub-microsecond resolution. The ultrasound interface IC used a high-voltage rail provided by an external power supply (5 to 36 V) to level-shift the low voltage transmit signal from the microcontroller to a high-voltage signal used to drive the external piezoelectric ultrasound transducer. Two different ultrasound transducers could be alternately used: one for interfacing with motes at shallow depth (12.7 mm diameter, 21.6 mm focal length, V306-SU-F0.85IN-PTF, Olympus NDT, Waltham MA), and one for interfacing with deep motes (25.4 mm diameter, 47.8 mm focal length, V304-SU-F1.88IN-PTF). For *in vivo* tests using these commercial, metal-encased transducers, a thin sheet of latex was stretched over the transducer face and castor oil was used as coupling between the transducer face and the latex. This prevented electrical paths from the stimulation site to external transceiver ground through the transducer casing. The electromechanical frequency response of the transducer filtered the square wave transmit signal resulting in a sinusoidal acoustic-domain signal. A single-element external transducer was chosen due to the ease and selection of commercial-off-the-shelf options. Depending on the clinical use case, a wearable external transceiver with a multi-element low-profile external transducer, as demonstrated in⁵⁵, may enable more convenient long-term stimulation and beamforming for fine-tuning of the beam axis relative to the mote position⁵⁷.

During UFIs (states A and G), the ultrasound interface chip switched from transmit (Tx) to receive (Rx) mode to pick up the backscattered signal captured by the external transducer. The receive signal was band-pass filtered and amplified (LT6203) by 4.8 dB. A 12-bit ADC on the microcontroller digitized the receive signal at 17 MSPS. The digitized backscatter was broken into two regions based on the timing values of the downlink modulation signal. The first backscatter region, $x_{S,n-1}$, was captured

immediately after the transceiver S_{n-1} to A_n transition and had a duration of twice the acoustic time-of-flight (TOF) between the external transducer and the mote ($\sim 20 \mu\text{s}$ to $60 \mu\text{s}$ depending on mote depth). This corresponded to the duration when the external transducer was no longer driven, but the acoustic wave was still travelling to and reflecting off the mote. The $x_{S,n-1}$ region had an amplitude dependent on the mote modulation state during the mote S period, which corresponded to the mote M_{mod} off. The second backscatter region, $x_{W,n}$, was captured immediately after the transceiver W_n to G_n transition and also had a duration of two TOF. This region had an amplitude dependent on the mote modulation state during the mote W period. When the mote was properly stimulating, M_{mod} was on during this region, otherwise M_{mod} was off. When turned on, M_{mod} reduced the electrical impedance seen by the mote piezo (Supplementary Fig. 1), reducing the amplitude of the backscattered wave.

To detect the modulation or uplink data for each pulse n (d_n), the normalized difference between the time-integrated amplitudes (L1 norms) of the $x_{W,n}$ and $x_{S,n-1}$ backscatter signals were compared to a threshold.

$$d_n = \frac{\|x_{W,n}\|_1 - \|x_{S,n-1}\|_1}{\|x_{S,n-1}\|_1} < \text{thresh}$$

The normalization canceled out any variation due to downlink power or path loss. With calibration, a threshold was determined which separates the backscatter relative difference into “1” bits below the threshold and “0” bits above the threshold. Either the L1 norm (volt-seconds) or the L2 norm (backscatter energy in Joules) could be used for this comparison, but L1 showed slightly better separation between backscatter states. This single-bit backscattered data from the mote, which signified whether the mote was stimulating or not, was given as feedback to the operator of the handheld external interrogator via an LED when the mote was detected as active. The backscatter bit and raw backscatter digitized waveforms could also be streamed to a PC via a serial connection for further logging and diagnostics, though this was not necessary for normal operation (backscatter data presented in the figures came from this offload connection).

Characterization of motes in ultrasound gel tissue phantom: To assess performance of the system, a mote with test leads was placed in ultrasound gel (Aquasonic Clear, Parker Labs, Fairfield NJ), either freely-floating or mounted on top of a $700 \mu\text{m}$ diameter steel rod connected to a rotation stage (RP01, Thorlabs, Newton, NJ). Bubbles were removed from all ultrasound gel used in this study via centrifugation for 16 minutes at $428 \times g$ to $1052 \times g$. Ultrasound gel has acoustic impedance and attenuation within 0.7% and 1.9%, respectively, of those of water⁵⁸. An electrical load was attached to

the mote electrode terminals to mimic tissue electrical properties (series 3 k Ω and 22 nF were used; note that in-vivo values were $R_{\text{Soln}} = \sim 4.54$ k Ω and $C_{\text{dl}} = \sim 17.9$ nF). The external transceiver was mounted to a computer-controlled 2-axis stage (XSlide, VelMex) with the external transducer contacting the gel. Mote parameter encoding and decoding performance were assessed at a mote depth of 18 mm using the 12.7 mm diameter external transducer at a transmit voltage of 19.4 V_{pk-pk}. Stimulation, power and backscatter performance were assessed at a mote depth of 48 mm using the 25.4 mm diameter external transducer at a transmit voltage of 25.6 V_{pk-pk}. Backscatter modulation uplink performance was assessed by determining the separation of demodulated ‘one’ bits and ‘zero’ bits. ‘One’ bits were gathered with a fully-powered mote showing a high relative difference between the modulation states (M_{mod} off during S_{n-1} and M_{mod} on during W_n). ‘Zero’ bits were gathered by operating a mote slightly underpowered so that stimulation did not occur and there was a low relative difference between the modulation states (M_{mod} off during S_{n-1} and M_{mod} off during W_n). The performance of the system at various positions and alignments of the mote in the acoustic link were assessed by rastering over the transverse translational and angular offset dimensions at a depth of 48 mm with the 25.4 mm diameter external transducer. The performance of the system at various depths and at high pulse repetition frequency were assessed with the mote on the central axis of the external transducer using the 25.4 mm diameter external transducer at a transmit voltage of 31.5 V_{pk-pk}. The external transceiver acoustic field for each transducer was characterized in a separate experiment in a water tank using a hydrophone (HGL-0400, Onda, Sunnyvale CA USA).

In vivo extracellular electrophysiological stimulation: All *in vivo* procedures were performed in accordance with University of California-Berkeley Animal Care and Use Committee regulations. Wireless stimulation was performed in 4 animals. For each procedure, a male Long-Evans rat (Charles River, Wilmington, MA) of approximately 300 g was anesthetized with 1250 mg/kg ethyl carbamate and placed on an isoflurane vaporizer at 0.5% isoflurane and 300 mL/minute flow rate. The skin around the leg was shaved and depilated. A semicircular flap incision was made from approximately the midpoint of the tibia to the midpoint of the femur, following the curvature of the knee joint. The biceps femoris was longitudinally bisected and resected to uncover the sciatic nerve. The fascia holding the sciatic nerve to the underlying musculature was removed, but the epineurium was left intact. The area was irrigated with sterile saline to ensure good electrical contact between the mote and the nerve. A mote was placed on the nerve approximately 4 mm proximal to the bifurcation of the nerve to innervate the limb extremities. The mote had 5 test leads attached to it for data collection purposes (GND, $V_{\text{Pz+}}$, $V_{\text{Pz-}}$, V_{DD} , V_{elec}) (Fig. 1c). These leads were unnecessary for the function of the mote and were used

for debugging, recording wired data to compare with the wireless readout for characterization purposes, and to standardize the fine-alignment of the acoustic link; they provided no power or communication signals to the mote. To ensure that these leads had no effect on the performance of the system, they were completely disconnected from all external instrumentation during a test trial and no change in system performance was seen.

For initial verification of functional stimulation and sweeps of stimulation current and pulse width, the surgical site was left open and the external interrogator was mounted such that the external transducer face was approximately 20 mm from the mote, with ultrasound gel filling the intervening space. The external interrogator was then turned on and chip V_{DD} was measured from test leads on the mote. The external interrogator position was adjusted to ensure good fine-alignment with the mote and successful stimulation was verified with test leads on the mote. This use of a measure of V_{DD} for fine alignment of the mote was used for repeatability between trials but was not necessary for function of the system. To verify this, positioning of the external transducer relative to the mote was performed without using V_{DD} as an alignment reference and the mote was able to receive enough power to function. The backscatter amplitude was also an option to aid in positioning the mote without use of a V_{DD} measurement.

Two penetrating stainless-steel electrodes were placed in the gastrocnemius muscle to capture the electromyogram signal (EMG) induced by sciatic nerve stimulation. The EMG signal was amplified by 1000X, bandpass filtered at 10 Hz to 3 kHz (DP-304, Warner Instr. Co., Hamden CT), and digitized at 100 kSPS (NI DAQ USB 6001, NI, Austin TX).

The external interrogator was programmed to specify a stimulation current, pulse width, and pulse repetition frequency. The system was initiated and performed approximately 30 to 60 stimulation events per condition before being set to different stimulation parameters. The pulse repetition frequency was kept at a relatively low $\sim 1/3$ Hz while generating recruitment curves to prevent muscle fatigue. Stimulation of the sciatic nerve elicited compound muscle action potentials (CMAP) across much of the lower leg musculature. CMAP amplitudes were calculated from baseline to the first peak. To calibrate the stimulation response curve, mote parameters were swept across stimulation current and stimulation pulse width dimensions, and baseline-to-peak CMAP amplitudes were calculated to construct a recruitment curve. A sweep of pulse repetition frequency was also performed and qualitative muscle response recorded.

To verify that the acoustic link was functional while transmitting through the tissue layer of the animal, the experiment was repeated with a closed surgical site. Excess ultrasound gel was removed, the biceps

femoris replaced over the nerve and mote, and the skin incision sutured with 6-0 nylon suture. With the wound closed, ultrasound gel was applied to the outside of the animal and the external interrogator was repositioned with the external transducer in contact with gel so that the distance from transducer to mote was 18 mm, with approximately 5 mm consisting of tissue. Downlink, stimulation, and uplink performance were then assessed with the fully implanted mote.

To characterize *in vivo* telemetry, backscatter modulation was detected as described above. The relative difference between the L1 norms of these two regions was calculated for 111 successful *in vivo* stimulation pulses (Fig. 6e left population). The relative difference between the L1 norms of the S_n and S_{n+1} backscatter regions was calculated for the same 111 pulses (Fig. 6e right population) and was used as an estimate of the backscatter when M_{mod} does not turn on during the W phase (which is the case when the mote does not stimulate).

Data Availability: All data used to draw conclusions are presented in this paper and associated Supplementary Information. Raw, pre-analyzed data is available upon request.

Computer Code Availability: All code used for programming the external transceiver and for analyzing data is available upon request.

Competing Interests: M.M.M., J.M.C., R.M.N, and J.E.K. are members of iota Biosciences, Inc.

References

1. Michelson, R. P. Electrical Stimulation of the Human Cochlea: A Preliminary Report. *Arch. Otolaryngol. - Head Neck Surg.* **93**, 317–323 (1971).
2. Birmingham, K. *et al.* Bioelectronic medicines: A research roadmap. *Nat. Rev. Drug Discov.* **13**, 399–400 (2014).
3. Plachta, D. T. T. *et al.* Blood pressure control with selective vagal nerve stimulation and minimal side effects. *J. Neural Eng.* **11**, (2014).
4. Koopman, F. A. *et al.* Vagus nerve stimulation inhibits cytokine production and attenuates disease severity in rheumatoid arthritis. **113**, (2016).
5. Bruns, T. M., Weber, D. J. & Gaunt, R. A. Microstimulation of Afferents in the Sacral Dorsal Root Ganglia Can Evoke Reflex Bladder Activity. *Neurourol Urodyn.* **34**, 65–71 (2015).
6. Zimmerman, L. L., Rice, I. C., Berger, M. B. & Bruns, T. M. Tibial Nerve Stimulation to Drive Genital Sexual Arousal in an Anesthetized Female Rat. *J. Sex. Med.* **15**, 296–303 (2018).
7. Bonaz, B., Sinniger, V. & Pellissier, S. The vagus nerve in the neuro-immune axis:

- Implications in the pathology of the gastrointestinal tract. *Front. Immunol.* **8**, (2017).
8. Tan, D. W. *et al.* A neural interface provides long-term stable natural touch perception. *Sci. Transl. Med.* **6**, (2014).
 9. Ajiboye, A. B. *et al.* Restoration of reaching and grasping movements through brain-controlled muscle stimulation in a person with tetraplegia: a proof-of-concept demonstration. *Lancet* **389**, 1821–1830 (2017).
 10. Chakravarthy, K., Nava, A., Christo, P. J. & Williams, K. Review of Recent Advances in Peripheral Nerve Stimulation (PNS). *Curr. Pain Headache Rep.* **20**, (2016).
 11. Benabid, A. L. *et al.* Long-term suppression of tremor by chronic stimulation of the ventral intermediate thalamic nucleus. *Lancet* **337**, 403–406 (1991).
 12. Widge, A. S., Malone, D. A. & Dougherty, D. D. Closing the loop on deep brain stimulation for treatment-resistant depression. *Front. Neurosci.* **12**, 1–10 (2018).
 13. Santacruz, S. R., Rich, E. L., Wallis, J. D. & Carmena, J. M. Caudate Microstimulation Increases Value of Specific Choices. *Curr. Biol.* **27**, 3375–3383.e3 (2017).
 14. Venkatraman, S. & Carmena, J. M. Active sensing of target location encoded by cortical microstimulation. *IEEE Trans. Neural Syst. Rehabil. Eng.* **19**, 317–324 (2011).
 15. Dadarlat, M. C., O’Doherty, J. E. & Sabes, P. N. A learning-based approach to artificial sensory feedback leads to optimal integration. *Nat. Neurosci.* **18**, 138–144 (2015).
 16. Medtronic. Medtronic Activa 37601. *English* (2008).
 17. Time, F. D. & Confidential, M. Intellis™ Rechargeable neurostimulator Implant manual Rx only M946871A001. (2012).
 18. RNS® System User Manual. (2015).
 19. Moro, E. Neurosurgery: Complications of DBS surgery-insights from large databases. *Nat. Rev. Neurol.* **12**, 617–618 (2016).
 20. Restaino, S. M., Abliz, E., Wachrathit, K., Krauthamer, V. & Shah, S. B. Biomechanical and functional variation in rat sciatic nerve following cuff electrode implantation. *J. Neuroeng. Rehabil.* **11**, 1–10 (2014).
 21. Wang, Y., Vaddiraju, S., Gu, B., Papadimitrakopoulos, F. & Burgess, D. J. Foreign body reaction to implantable biosensors: Effects of tissue trauma and implant size. *J. Diabetes Sci. Technol.* **9**, 966–977 (2015).
 22. Tanabe, Y. *et al.* High-performance wireless powering for peripheral nerve neuromodulation systems. *PLoS One* **12**, 1–13 (2017).
 23. Freeman, D. K. *et al.* A sub-millimeter, inductively powered neural stimulator. *Front. Neurosci.* **11**, 1–12 (2017).
 24. Lee, H. M., Kwon, K. Y., Li, W. & Ghovanloo, M. A power-efficient switched-capacitor stimulating system for electrical/optical deep brain stimulation. *IEEE J. Solid-State Circuits* **50**, 360–374 (2015).
 25. Lee, B. *et al.* An Implantable Peripheral Nerve Recording and Stimulation System for Experiments on Freely Moving Animal Subjects. *Sci. Rep.* **8**, 1–12 (2018).

26. Lin, Y. P. *et al.* A Battery-Less, Implantable Neuro-Electronic Interface for Studying the Mechanisms of Deep Brain Stimulation in Rat Models. *IEEE Trans. Biomed. Circuits Syst.* **10**, 98–112 (2016).
27. Seo, D., Carmena, J. M., Rabaey, J. M., Alon, E. & Maharbiz, M. M. Neural Dust: An Ultrasonic, Low Power Solution for Chronic Brain-Machine Interfaces. *arXiv.org q-NC*, (2013).
28. Seo, D., Carmena, J. M., Rabaey, J. M., Maharbiz, M. M. & Alon, E. Model validation of untethered, ultrasonic neural dust motes for cortical recording. *J. Neurosci. Methods* **244**, 114–122 (2015).
29. Seo, D. *et al.* Wireless Recording in the Peripheral Nervous System with Ultrasonic Neural Dust. *Neuron* **91**, 529–539 (2016).
30. Charthad, J., Weber, M. J., Chang, T. C. & Arbabian, A. A mm-Sized Implantable Medical Device (IMD) With Ultrasonic Power Transfer and a Hybrid Bi-Directional Data Link. *IEEE J. Solid-State Circuits* **50**, 1741–1753 (2015).
31. Luo, Y. S. *et al.* Ultrasonic power/data telemetry and neural stimulator with OOK-PM signaling. *IEEE Trans. Circuits Syst. II Express Briefs* **60**, 827–831 (2013).
32. Charthad, J. *et al.* A mm-Sized wireless implantable device for electrical stimulation of peripheral nerves. *IEEE Trans. Biomed. Circuits Syst.* **12**, 257–270 (2018).
33. Thimot, J. & Shepard, K. L. Bioelectronic devices: Wirelessly powered implants. *Nat. Biomed. Eng.* **1**, 1–2 (2017).
34. FDA. Information for Manufacturers Seeking Marketing Clearance of Diagnostic Ultrasound Systems and Transducers. 1–64 (2008). Available at: <https://www.fda.gov/downloads/UCM070911.pdf>.
35. Johnson, B. C. *et al.* StimDust : A 6.5mm³ , Wireless Ultrasonic Peripheral Nerve Stimulator with 82% Peak Chip Efficiency. *Cicc* 8–11 (2018). doi:10.1109/CICC.2018.8357047
36. Johnson, B. C. *et al.* An implantable 700μW 64-channel neuromodulation IC for simultaneous recording and stimulation with rapid artifact recovery. *IEEE Symp. VLSI Circuits, Dig. Tech. Pap.* C48–C49 (2017). doi:10.23919/VLSIC.2017.8008543
37. Weitz, A. C., Behrend, M. R., Humayun, M. S., Chow, R. H. & Weiland, J. D. Interphase gap decreases electrical stimulation threshold of retinal ganglion cells. *Proc. Annu. Int. Conf. IEEE Eng. Med. Biol. Soc. EMBS* 6725–6728 (2011). doi:10.1109/IEMBS.2011.6091658
38. Weitz, A. C. *et al.* Interphase gap as a means to reduce electrical stimulation thresholds for epiretinal prostheses. *J. Neural Eng.* **11**, (2014).
39. Stanslaski, S. *et al.* Design and validation of a fully implantable, chronic, closed-loop neuromodulation device with concurrent sensing and stimulation. *IEEE Trans. Neural Syst. Rehabil. Eng.* **20**, 410–421 (2012).
40. Yamamoto, T., Fukaya, C., Yoshino, A. & Katayama, Y. Instrument of Brain Stimulation. in *Deep Brain Stimulation for Neurological Disorders: Theoretical Background and Clinical Application* (ed. Itakura, T.) 49–60 (Springer International Publishing, 2015). doi:10.1007/978-3-319-08476-3_5

41. Martin, A. J. *et al.* Placement of deep brain stimulator electrodes using real-time high-field interventional magnetic resonance imaging. *Magn. Reson. Med.* **54**, 1107–1114 (2005).
42. Azhari, H. Appendix A: Typical Acoustic Properties of Tissues. *Basics Biomed. Ultrasound Eng.* 313–314 (2010). doi:10.1002/9780470561478.app1
43. Nassiri, D. K., Nicholas, D. & Hill, C. R. Attenuation of ultrasound in skeletal muscle. *Ultrasonics* **17**, 230–232 (1979).
44. Ayaz, M. *et al.* Sexual dependency of rat sciatic nerve fiber conduction velocity distributions. *Int. J. Neurosci.* **117**, 1537–49 (2007).
45. Celichowski, J. Mechanisms underlying the regulation of motor unit contraction in the skeletal muscle. *Journal of Physiology and Pharmacology* **51**, 17–33 (2000).
46. Bhadra, N., Bhadra, N., Kilgore, K. & Gustafson, K. J. High frequency electrical conduction block of the pudendal nerve. *J. Neural Eng.* **3**, 180–187 (2006).
47. Khalifa, A. *et al.* The Microbead: A Highly Miniaturized Wirelessly Powered Implantable Neural Stimulating System. *IEEE Trans. Biomed. Circuits Syst.* **12**, 521–531 (2018).
48. Alexandrov, A. V. *et al.* Ultrasound-Enhanced Systemic Thrombolysis for Acute Ischemic Stroke. *N. Engl. J. Med.* **351**, 2170–2178 (2004).
49. Baron, C., Aubry, J. F., Tanter, M., Meairs, S. & Fink, M. Simulation of Intracranial Acoustic Fields in Clinical Trials of Sonothrombolysis. *Ultrasound Med. Biol.* **35**, 1148–1158 (2009).
50. Venkatraman, S. *et al.* In Vitro and In Vivo Evaluation of PEDOT Microelectrodes for Neural Stimulation and Recording. **19**, 307–316 (2011).
51. Hassler, C., Boretius, T. & Stieglitz, T. Polymers for neural implants. *J. Polym. Sci. Part B Polym. Phys.* **49**, 18–33 (2011).
52. Barrese, J. C. *et al.* Failure mode analysis of silicon-based intracortical microelectrode arrays in non-human primates. *J. Neural Eng.* **10**, (2013).
53. Fang, H. *et al.* Ultrathin, transferred layers of thermally grown silicon dioxide as biofluid barriers for biointegrated flexible electronic systems. *Proc. Natl. Acad. Sci.* **113**, 11682–11687 (2016).
54. Diaz-Botia, C. A. *et al.* A silicon carbide array for electrocorticography and peripheral nerve recording. *J. Neural Eng.* **14**, (2017).
55. Piech, D. K., Kay, J. E., Boser, B. E. & Maharbiz, M. M. Rodent wearable ultrasound system for wireless neural recording. *Proc. Annu. Int. Conf. IEEE Eng. Med. Biol. Soc. EMBS* 221–225 (2017). doi:10.1109/EMBC.2017.8036802
56. Tang, H.-Y., Lu, Y., Fung, S., Horsley, D. A. & Boser, B. E. 11.8 Integrated ultrasonic system for measuring body-fat composition. in *2015 IEEE International Solid-State Circuits Conference - (ISSCC) Digest of Technical Papers* 1–3 (IEEE, 2015). doi:10.1109/ISSCC.2015.7063000
57. Seo, D. *et al.* Ultrasonic Beamforming System for Interrogating Multiple Implantable Sensors. *2015 37th Annu. Int. Conf. IEEE Eng. Med. Biol. Soc.* 1–4 (2015). doi:10.1109/EMBC.2015.7318942

58. Casarotto, R. A., Adamowski, J. C., Fallopa, F. & Bacanelli, F. Coupling Agents in Therapeutic Ultrasound: Acoustic and Thermal Behavior. *Arch. Phys. Med. Rehabil.* **85**, 162–165 (2004).
59. Jiménez, N. *et al.* Nonlinear Acoustics FDTD method including Frequency Power Law Attenuation for Soft Tissue Modeling. *arXiv* (2014).
60. Ye, P. P., Brown, J. R. & Pauly, K. B. Frequency dependence of ultrasound neurostimulation in the mouse brain. *Ultrasound Med. Biol.* **42**, 1512–1530 (2016).
61. Downs, M. E. *et al.* Non-invasive peripheral nerve stimulation via focused ultrasound *in vivo*. *Phys. Med. Biol.* (2017). doi:10.1088/1361-6560/aa9fc2

Supplemental Information

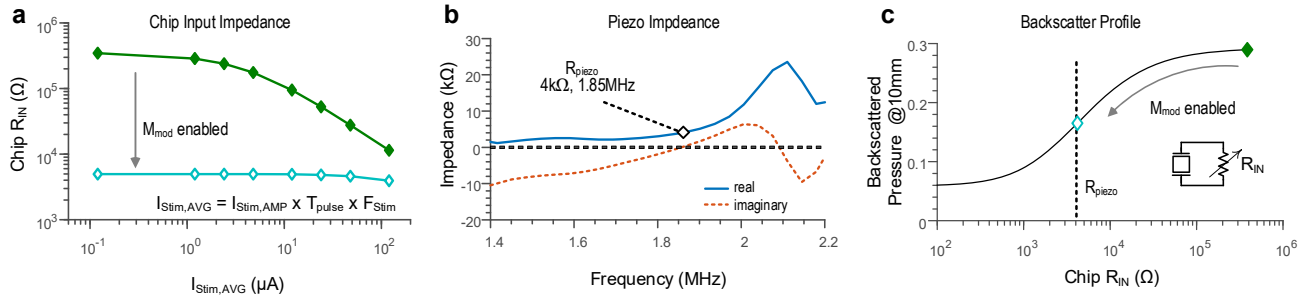


Fig. S1 | Backscatter modulation design. **a**, The measured chip input resistance (R_{IN}) for different current stimulation loads. The bottom trace is when the modulation switch is enabled, keeping R_{IN} constant across load. The difference between the two lines is the modulation depth for a given load. **b**, Simulated mote piezo impedance versus frequency. At resonance, the piezo has a 4 k Ω impedance. **c**, Simulated backscatter profile at 10mm based for different R_{IN} .

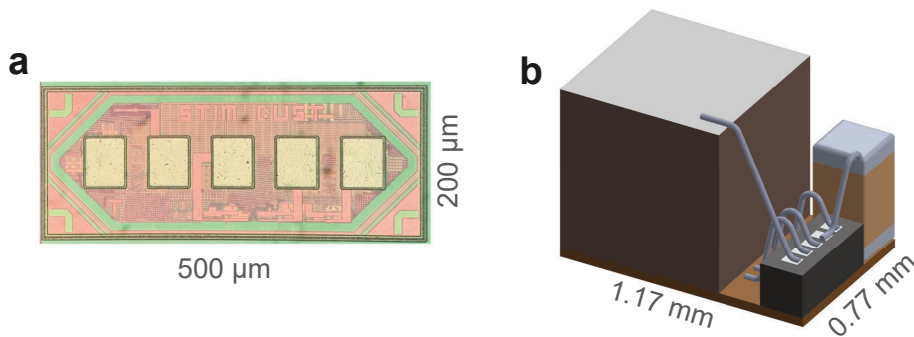


Fig. S2 | Further miniaturized StimDust mote. **a**, fabricated further-miniaturized StimDust IC. **b**, Design of further-miniaturized mote utilizing the fabricated IC and a piezo of the same dimensions as that in Fig 4.

Supplementary Section 1: Additional results from characterizing mote performance in a gel tissue phantom

The step response ring-up time of the external transducer was approximately 1 cycle, or 0.56 μ s. The ring-up time for the external transducer and mote piezo system (full downward link) was approximately 3.5 cycles or 1.94 μ s. The ring-up time for the external transducer, mote piezo, and backscatter capture system (full bidirectional link) was approximately 4.5 cycles or 2.5 μ s. A pulse-train mode was demonstrated by interspersing several pulses of short-duration shorting-phase with a pulse of long-

duration shorting-phase. This yielded a pulse-train every 500 ms, with each train containing 10 pulses of 100 μ s pulse width occurring every 750 μ s.

The acoustic beam patterns of the 12.7 mm and 25.4 mm diameter external transducers (Supplementary Fig. 3) were had a focal plane intensity transverse full-width-half-maximum of 1.6 mm and 1.8 mm, respectively, and an axial intensity longitudinal full-width-half-maximum of 14 mm and 17.7 mm.

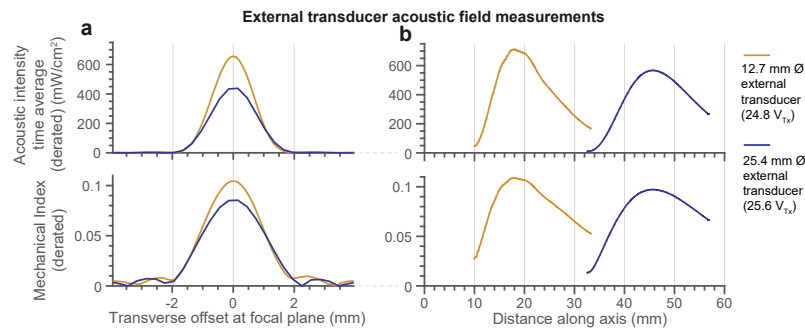


Fig. S3 | External transceiver acoustic field. Characterization of the external transducer acoustic field for two alternate transducers used for shallow (12.7 mm diameter transducer) and deep operation (25.4 mm diameter transducer). Data taken in a water tank with external transceiver and hydrophone.

The power performance of the system was measured for two conditions: benchtop operation at high PRF and *in vivo* operation with a fully implanted mote at low PRF (Supplementary Table 1). V_{TX} and $P_{electrical}$ into the external transducer were measured at the output of the external power supply used to supply the ultrasound interface chip. The external transducer was heavily damped to shorten its impulse response and much of the acoustic power generated in the external transducer piezo was dumped into the absorptive backing layer, causing the electrical input power to acoustic power at the focal plane efficiency to be low.

Acoustic domain measurements were made with a hydrophone in water; notably, the hydrophone measurements were taken in a separate experiment from mote operation and the acoustic values in table 1 assume that the mote was positioned at the point of maximal acoustic intensity (this may cause up to ~20% error). For the *in vivo* condition, the hydrophone measurements could not be made directly, and so expected loss from impedance mismatches and absorption in 2 mm of skin and 3 mm of muscle (^{42, 59, 43}) was modeled to yield an estimate of acoustic intensity inside the animal. The acoustic power at the focal plane (depth of the mote) was integrated over a 1 cm radius circle, which is at least 97% of

the total power in the focal plane. The face of the mote captured approximately 20% of the acoustic power in the focal plane. This was a trade-off that balances minimizing the power coupling sensitivity of small transverse misalignments with minimizing the unused ultrasound power radiating into the body.

The acoustic power conversion efficiency (η_{acoustic}) is defined as the ratio of the electrical power used to charge to the mote relative to the acoustic power at the face of the mote piezo. This efficiency encompasses the acoustic to electrical power efficiency of the piezo, the rectifier efficiency, and the standby power consumption of the IC. It was calculated from the measured rate of change of the C_{store} capacitor voltage (V_{DD}) during initial mote power-up for a 3V V_{DD} steady-state. Under a given incident acoustic power, the η_{acoustic} (as measured by P into C_{store}) peaked at $\sim 8.1\%$ when V_{DD} was near half the steady-state voltage (Fig. 6f, Supplementary Fig. 4). The mote's stimulation power ($P_{\text{stimulation_delivered}}$) was calculated by measuring the voltage across an electrode model load. The electrode load was modeled as a solution resistance (R_{soln}) and double-layer capacitance (C_{dl}) in series. R_{soln} and C_{dl} were discrete passives for the benchtop test; *in vivo* values were estimated from the stimulation voltage at known current output by using the initial IR drop and initial slope of capacitive charging. Q_{pulse} (charge per pulse), E_{pulse} , and $P_{\text{stimulation_delivered}}$ were calculated from the measured stimulation voltage waveform, R_{soln} , C_{dl} , and f_{stim} . $P_{\text{stimulation_available}}$ was calculated from Q_{pulse} delivered, the voltage headroom available, and f_{stim} . $P_{\text{stimulation_delivered}}$ represents the power delivered to the electrode model used (and would change with load) while $P_{\text{stimulation_available}}$ represents the maximum stimulation power available for any load.

Note that at low PRF the total $P_{\text{stimulation_delivered}}$ was low and the device charged up quickly and remained 'idle' for most of the time between stimulation pulses yielding a low overall efficiency. Under low PRF conditions, it was shown that the device could be intermittently powered up for each pulse to reduce the overall ultrasound dose. If optimized for this application, the mote could have a small C_{store} to reduce startup time.

Table S1: System power performance

	Benchtop high PRF example	<i>In vivo</i> low PRF example
Acoustic medium	ultrasound gel	gel, skin, muscle
Mote depth from ext. txdr	48 mm	18 mm
Stimulation protocol		
Specified PRF	2380 Hz	.222 Hz
Specified stim current	400 μ A	400 μ A
Specified stim pulse width	72 μ s	172 μ s
Specified interphase gap	10 μ s	80 μ s
External transceiver		
External transducer	25.4 mm \emptyset	12.7 mm \emptyset
V_{TX}	28.9 V	24.8 V
U/S duty cycle with UFI's	76%	100%
$P_{\text{electrical}}$ drive ext. txdr	2.0 W	1.34 W
I_{SPTA} derated	723 mW/cm ²	713 mW/cm ²
P_{acoustic} focal plane 1 cm rad.	20.8 mW	14.6 mW
P_{acoustic} on mote piezo face	4.3 mW	2.8 mW
Mote		
Mote C_{store}	4 μ F	4 μ F
V_{DD} steady state	1.9 V	3.0 V
P into C_{store} average	147 μ W*	9.7 μ W
η_{acoustic}	3.4%*	0.34%
Load		
Load R_{soln} (est. for <i>in vivo</i>)	3 k Ω	4.4 k Ω
Load C_{dl} (est. for <i>in vivo</i>)	22 nF	17.9 nF
Q_{pulse}	24 nC	43.4 nC
E_{pulse}	37 nJ	108 nJ
$P_{\text{stimulation_delivered}}$	89 μ W	24 nW
$P_{\text{stimulation_available}}$	103 μ W	30 nW

* these power values were derived based on the incident acoustic power at the mote face and the measured efficiencies at various V_{DDs} .

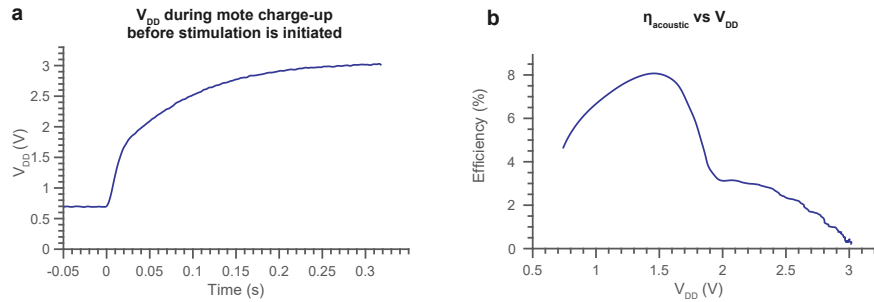
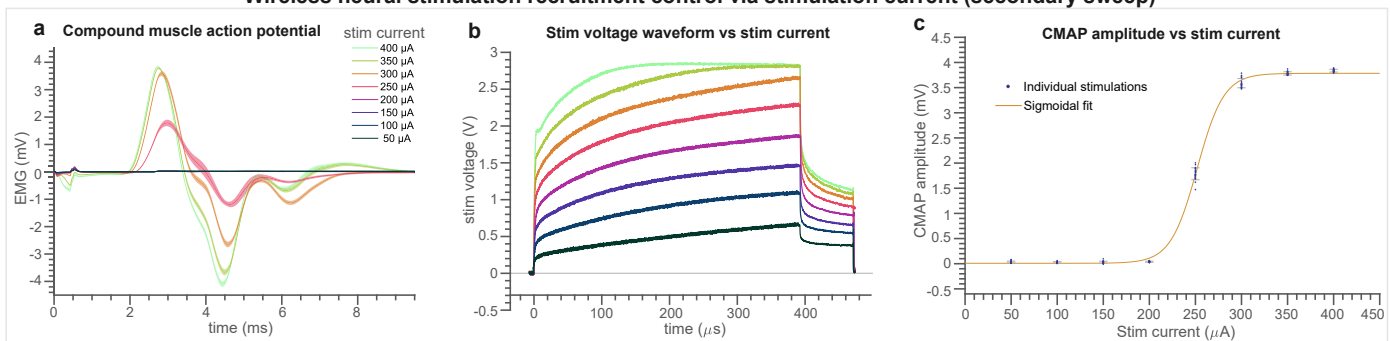


Fig. S4 | *In vivo* power harvesting performance during initial power-up. **a**, After 4.2 s without receiving power, the mote V_{DD} (V across C_{store}) was ~ 0.7 V. When downlink power resumed (at $t = 0$), the $4 \mu\text{F}$ C_{store} charged over ~ 300 ms. **b**, The charging waveform from (a) was used to estimate the efficiency during charging as V_{DD} passed through various regimes. $\eta_{acoustic}$ is the ratio of electrical power used for charging the mote to acoustic power at the face of the mote piezo. At $1.2 V_{DD}$, the rate of electrical power harvest was maximum but V_{DD} was below the POR cutoff and the device did not stimulate. Between $1.9 V_{DD}$ and $3.0 V_{DD}$, the mote was able to stimulate. Power harvest efficiency was moderate at $1.9 V_{DD}$ and decreased to very low values at $3.0 V_{DD}$, which was the point where C_{store} was nearly topped off and ‘trickle charging’ under the given incident acoustic power conditions.

Wireless neural stimulation recruitment control via stimulation current (secondary sweep)



Wireless neural stimulation recruitment control via stimulation pulse duration (secondary sweep)

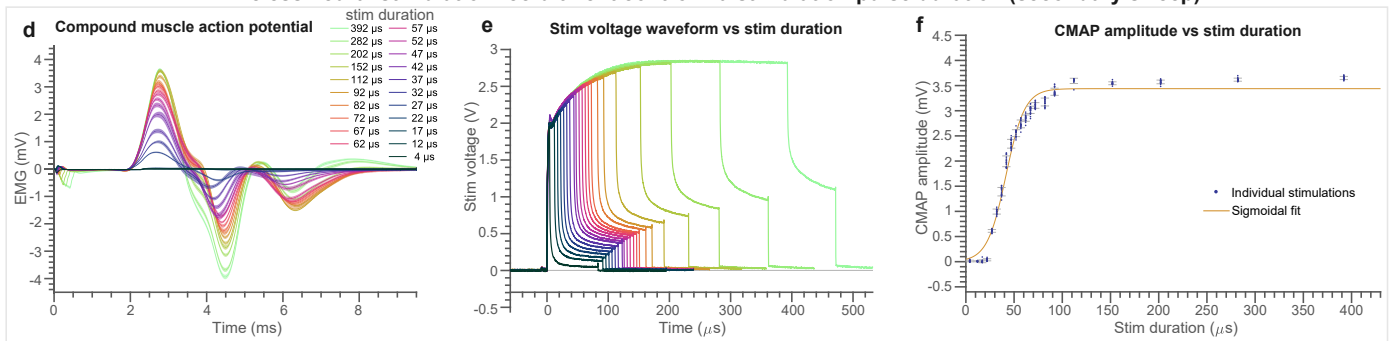


Figure S5: Precise control of evoked neural response achieved through varying stimulation current or stimulation pulse width, second sweep of parameters: This data was taken with the same animal and mote as that in Fig. 7, but 2 hours after the first sweep. See Fig. 7 for panel descriptions.

Supplementary Section 2: Discussion supporting the claim that stimulation was due to the mote output current and was not directly ultrasound mediated

At 1.85 MHz, the threshold of ultrasound-mediated neural stimulation has been reported at approximately 10 W/cm^2 pulse-average intensity⁶⁰; this is more than 14x higher intensity than that used in this study. Furthermore, as the system increased stimulation current from 50 μA to 400 μA with a corresponding recruitment of CMAP response, acoustic power was nearly identical and actually decreased slightly since the protocol utilizes a longer TDC gap when specifying high current. Additionally, no EMG response was observed when the system was driven with continuous ultrasound at the same intensity as used for controlling the device, but with no coded downlink signals. Finally, a pilot *in vivo* experiment, which powered the mote electrically with no ultrasound, produced stimulation and evoked CMAP's identical to those evoked with an acoustically-powered mote (data not shown). Utilizing a current-control implantable stimulator provides improved stimulation precision and spatial resolution as compared to directly mediated ultrasonic stimulation, and requires substantially lower acoustic intensities and thus has lower risk from ultrasound-induced thermal or cavitation damage⁶¹.

Video S1 | In vivo neural stimulation with fully implanted wireless StimDust. Example stimulation pulses delivered at $\sim 0.25 \text{ Hz}$. In the first two clips, the animal's right hindquarters are visible with cranial to the right and caudal to the left. The closed surgical site is at the center of the frame and the animal's right leg and foot are towards the bottom left of the frame, with two EMG electrodes visible. The external transducer can be seen at the top of the frame. Ultrasound gel fills the gap between the external transducer and the animal, and a glass slide makes this space visible. The third clip shows a view from the rear. The fourth clip shows a different experiment with the mote implanted on the left sciatic.